

Defect Induced Asymmetric Pit Formation on Hydroxyapatite

Ki-Young Kwon,[†] Eddie Wang,[†] Alice Chung,[†] Neil Chang,[†] Eduardo Saiz,[‡] Uh-Joo Choe,[§] Maxwell Koobatian,^{||} and Seung-Wuk Lee^{*†}

Department of Bioengineering, University of California, Berkeley, California 94720, Physical Biosciences Division, Lawrence Berkeley National Laboratory, Berkeley, California 94720, Berkeley Nanoscience and Nanoengineering Institute, Berkeley, California 94720, Materials Sciences Division, Lawrence Berkeley National Laboratory, Berkeley, California 94720, Department of Bioengineering, University of California, Los Angeles, California 90095, and Department of Chemistry, University of California, Merced, California 95344

Received June 4, 2008. Revised Manuscript Received July 28, 2008

Defect sites on bone minerals play a critical role in bone remodeling processes. We investigated single crystal hydroxyapatite (100) surfaces bearing crystal defects under acidic dissolution conditions using real-time in situ atomic force microscopy. At defect sites, surface structure-dependent asymmetric hexagonal etch pits were formed, which dominated the overall dissolution rate. Meanwhile, dissolution from the flat terraces proceeded by stochastic formation of flat bottom etch pits. The resulting pit shapes were intrinsically dictated by the HAP crystal structure. Computational modeling also predicted different step energies associated with different facets of the asymmetric etch pits. Our microscopic observations of HAP dissolution are significant for understanding the effects of local surface structure on the bone mineral remodeling process and provide useful insights for the design of novel therapies for treating osteoporosis and dental caries.

Introduction

Bones are dynamic, mineralized tissues which undergo continuous cell-mediated remodeling by bone depositing osteoblasts and bone-resorbing osteoclasts.¹ A balanced remodeling process allows for the adaptation and maintenance of skeletal architecture and for the control of essential ion homeostasis, whereas an imbalance toward excess resorption can lead to conditions such as osteoporosis, osteolysis, and Paget's disease.² Consequently, a great deal of research and drug development has gone into understanding and suppression of osteoclast activity.³ However, less understood is the microscopic behavior of the inorganic bone mineral phase as it undergoes osteoclast mediated acid dissolution. The dissolution of bone mineral, known as biological apatite, has been difficult to characterize due to the complexity of the system (structurally diverse mixture of inorganic apatite mineral,⁴ organic macromolecules,^{5,6} extracellular matrix,⁷ cells,⁸ and ions) and the technological limitations associated with attaining a well-defined system for gathering precise measurements. To overcome these issues, dissolution of biological apatites

as well as hydroxyapatite^{9,10} (HAP), a close synthetic analog of biological apatite, have been studied under simplified acidic conditions in vitro.^{11–13} Several dissolution mechanisms have been proposed based on solution phase kinetic data by measuring transient calcium and phosphate ion concentrations from bulk solutions.^{14–16} However, bone resorption occurs on the apatite surfaces. Recent microscopic kinetic studies based on scanning probe microscopes have shown that the reactions taking place at the solid/liquid (or gas) interface, such as dissolution, nucleation, diffusion and catalytic reactions are significantly affected by local surface structural and stoichiometric environments.^{17–20} Therefore, the direct observation of atomically well-defined apatite surfaces can provide a fundamental understanding of how the inorganic components of bone and tooth resorb, which cannot be obtained from bulk solution experiments. Here, we report on microscopic dissolution of hydroxyapatite crystals in an acidic buffer solution environment by measuring individual molecular step kinetics on atomically flat surfaces using in situ AFM. Importantly, well-defined (100) HAP surfaces bearing various structural defects were monitored to investigate local structure-dependent dissolution processes. We found that local structural defects played an important role in the overall kinetics of HAP dissolution, and resulted in the formation of etch pits with

* To whom correspondence should be addressed. E-mail: leesw@berkeley.edu.

[†] University of California, Berkeley, Physical Biosciences Division, Lawrence Berkeley National Laboratory, and Berkeley Nanoscience and Nanoengineering Institute.

[‡] Materials Sciences Division, Lawrence Berkeley National Laboratory.

[§] University of California, Los Angeles.

^{||} University of California, Merced.

(1) Bronner, F.; Farach-Carson, M. C.; Rubin, J., *Bone resorption*; Springer: London, 2005; pp xiii, 189.

(2) Rodan, G. A.; Martin, T. J. *Science* **2000**, *289*, 1508.

(3) Teitelbaum, S. L. *Science* **2000**, *289*, 1504.

(4) Weiner, S.; Wagner, H. D. *Annu. Rev. Mater. Sci.* **1998**, *28*, 271.

(5) Gibson, J. M.; Raghunathan, V.; Popham, J. M.; Stayton, P. S.; Drobny, G. P. *J. Am. Chem. Soc.* **2005**, *127*, 9350.

(6) Capriotti, L. A.; Beebe, T. P.; Schneider, J. P. *J. Am. Chem. Soc.* **2007**, *129*, 5281.

(7) Eberhardt, E. S.; Panasik, N.; Raines, R. T. *J. Am. Chem. Soc.* **1996**, *118*, 12261.

(8) El-Ghannam, A. R.; Ducheyne, P.; Risbud, M.; Adams, C. S.; Shapiro, I. M.; Castner, D.; Gollidge, S.; Composto, R. J. *J. Biomed. Mater. Res. Part A* **2004**, *68*, 615.

(9) Kay, M. I.; Young, R. A.; Posner, A. S. *Nature* **1964**, *204*, 1050.

(10) Elliott, J. C., *Structure and chemistry of the apatites and other calcium orthophosphates*; Elsevier: Amsterdam, New York, 1994; pp xiii, 387.

(11) Brady, B. H. G.; Mapper, D. H.; Smythe, B. M. *Nature* **1966**, *212*, 77.

(12) Moreno, E. C.; Kresak, M.; Zahradni, R. *Nature* **1974**, *247*, 64.

(13) Valsami-Jones, E.; Ragnarsdottir, K. V.; Putnis, A.; Bosbach, D.; Kemp, A. J.; Cressey, G. *Chem. Geol.* **1998**, *151*, 215–233.

(14) Dorozhkin, S. V. *Prog. Cryst. Growth Charact. Mater.* **2002**, *44*, 45.

(15) Tang, R. K.; Nancollas, G. H.; Orme, C. A. *J. Am. Chem. Soc.* **2001**, *123*(23), 5437–5443.

(16) Tomson, M. B.; Nancollas, G. H. *Science* **1978**, *200*(4345), 1059.

(17) Schaub, R.; Wahlstrom, E.; Ronnau, A.; Laegsgaard, E.; Stensgaard, I.; Besenbacher, F. *Science* **2003**, *299*, 377.

(18) Kwon, K. Y.; Wong, K. L.; Pawin, G.; Bartels, L.; Stolbov, S.; Rahman, T. S. *Phys. Rev. Lett.* **2005**, *95*, 166101.

(19) Land, T. A.; DeYoreo, J. J.; Lee, J. D. *Surf. Sci.* **1997**, *384*, 136.

(20) Gratz, A. J.; Manne, S.; Hansma, P. K. *Science* **1991**, *251*, 1343.

asymmetric hexagonal morphologies which are governed by the HAP crystal structure.

Experimental Section

Synthesis and Characterization of HAP Crystal. Single crystal HAP was synthesized through molten salt synthesis.²¹ HAP powders (20.0 g, Alfa Aesar) were mixed with potassium sulfate (24.0 g, Aldrich). This mixture was placed inside a furnace, and heated to 1190 at 10 °C/min. After soaking for 3.5 h, the sample was cooled to ambient temperature at 10 °C/min. Finally, the mixture was washed four times with hot water (≈ 90 °C) and filtered to obtain HAP single-crystal whiskers. The crystalline phases of the HAP whiskers were evaluated by XRD (D500 instrument) using Cu K α radiation. The morphologies of the HAP crystals were observed using an environmental scanning electron microscope (Hitachi S-4300SE/N). HAP whiskers were coated with Au using a sputter coater (BAL-TEC, SCD 050) to obtain optimal imaging contrast.

AFM Experiments and Data Analysis. HAP crystals (< 3 μg) were glued onto glass substrates using an epoxy resin. This substrate was placed in the bottom of a fluid cell (volume ≈ 2 mL). All AFM images were taken under fluid conditions in contact mode using MFP3D AFM (Asylum research, Santa Barbara, CA). Initially, several images were obtained under deionized water. Except for the initial images, AFM images were obtained while flowing the acidic buffer (pH 6, 10 mM citrate) through the fluid cell. A syringe pump (KDS270, KS Scientific, Holliston, MA) was used to provide constant infusion and withdrawal of buffer solution at flow rates of 1–10 mL/hr. These rates were fast enough that dissolution was not affected by diffusion of the buffer (Under nonflow conditions, decreased dissolution rates were observed at least 6 h after injection of the same buffer). To ensure that the AFM tip did not alter the surface, scanning direction, size, angle, and force were varied. Dissolution rates of the terrace region were calculated by counting the removal of individual (100) layers based on successive AFM images. In etch pit regions, the dissolution rate was estimated by analyzing the widths, lengths, and vertical depths of the etch pits.

Molecular Modeling. To calculate theoretical step energies, step geometries were generated using GDIS²² and subjected to static lattice minimization using GULP.²³ Previously determined potential parameters for HAP developed by Filgueiras et al. were employed.²⁴ This potential model, based on the Born model of solids models ion interactions with long-range Coulombic terms and short-range Buckingham terms.²⁵ Covalent bonds are modeled using Morse potentials while a harmonic three-body term restrains the phosphate geometry. As an initial structure, the experimentally determined HAP unit cell parameters of Hughes et al., were used ($a = b = 9.417$ Å, $c = 6.874$ Å).²⁶ The partial occupancy of hydroxide ions in the unit cell was simplified for simulation by converting the structure to the P1 space group. Subsequently, selected hydroxide ions were removed such that the remaining hydroxides were aligned in the same direction.²⁷ The unit cell was then relaxed yielding the following lattice parameters: $a = b = 9.348$ Å and $c = 6.866$ Å. This relaxed unit cell was used to generate all subsequent surface geometries. For each surface geometry, six faces vicinal to the (100) surface were generated. The surfaces created were the $(n10)$ and $(-[n + 1], 10)$ surfaces where n equaled 2, 3, or 4. Atoms were then manually removed from the surfaces to create obtuse, (100) interlayer height step edges separated by (100) surface terraces. The length of the terrace regions between steps was dependent on n where $(n \times \text{unit cell } a \text{ parameter}) = \text{length of the terrace}$. The geometries were created so as to ensure neutral, nonpolar surfaces. Finally, these surfaces were subjected to energy minimization using

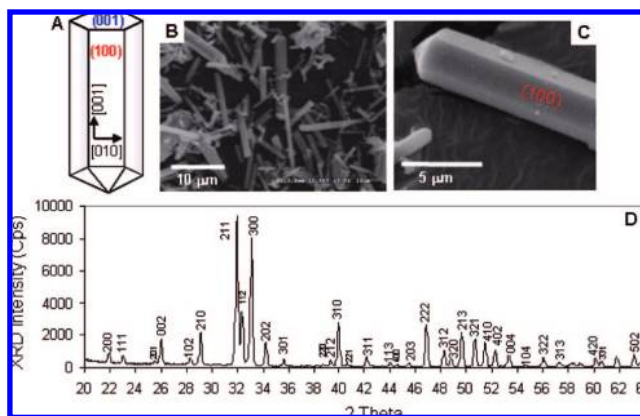


Figure 1. Characterization of single crystal HAP. (A) Model of HAP, Crystallographic axes and surfaces are defined. (B and C) SEM images of HAP. Crystals are elongated along the [001] direction. More than 95% of surface is covered by (100)-like surfaces. (D) XRD pattern of HAP crystals.

GULP. Using a method developed by Kristensen et al., the values determined by energy minimization allow for extrapolation of individual step energies.²⁸

Results and Discussions

Figure 1A–C shows a model and an SEM image of HAP whiskers prepared by molten salt synthesis. The crystals were elongated along the [001] direction, and consequently more than 95% of the surface was covered by six (100)-like surfaces that are physically and chemically identical. The XRD peaks are consistent with previous typical single crystal HAP patterns (Figure 1D).^{10,29} In addition, careful analysis of XRD patterns enabled us to verify the absence of α -tricalcium phosphate ($\text{Ca}_3(\text{PO}_4)_2$), a thermal decomposition residue of HAP, which is commonly found when overheating occurs during HAP molten salt synthesis.

Figure 2A shows an AFM image of HAP (100) surfaces under deionized water. Molecular steps were observed across the atomically flat terrace. Step a (upper region) and steps b and c were slightly tilted by less than 4° to the [001] and [011] directions, respectively. Cross-sectional analysis (Figure 2E and F) of the surface showed that the average heights of each of steps a–c were 0.83, 0.83, and 0.86 nm respectively, which are close to the interlayer distance of the (100) surface ($d(100) \approx 0.82$ nm). An important feature of the selected (100) HAP surface was the presence of various structural defects (Figure 2A). Eight small pinholes were observed (numbered in Figure 2A). Pinholes 1–6 were angled at less than 2° to the [010] direction and were spaced at similar intervals (≈ 220 nm), suggesting that each pinhole fell along an edge dislocation line where an extra half-plane was inserted along the [010] direction. Step c is terminated at pinhole 8, which was a screw dislocation site. We intentionally chose the HAP (100) surfaces exhibiting these structural defects because they allowed us to characterize the evolution of the dissolution process as a function of the local structural environment.

After exposure to acidic buffer, the dissolution of HAP (100) surfaces proceeded in a local structure-dependent manner. Rapid dissolution was observed at the structural defect sites (pinholes 1–8) (Figure 2B). At these edge and screw dislocation pinholes, deep etch pits with elongated hexagonal shapes were formed in

(21) Tas, A. C. *J. Am. Ceram. Soc.* **2001**, *84*, 295.

(22) Fleming, S., GDIS: GTK Display Interface for Structures, 0.89.

(23) Gale, J. D. *J. Chem. Soc. Faraday Trans.* **1997**, *93*, 629.

(24) Filgueiras, M. R. T.; Mkhonto, D.; de Leeuw, N. H. *J. Cryst. Growth* **2006**, *294*, 60.

(25) Born, M.; Huang, K. *Dynamical Theory of Crystal Lattices*; Oxford University Press: New York, 1959.

(26) Hughes, J. M.; Cameron, M.; Crowley, K. D. *Am. Mineral.* **1989**, *74*, 870.

(27) Mostafa, N. Y.; Brown, P. W. *J. Phys. Chem. Solids* **2006**, *68*, 431.

(28) Kristensen, R.; Stipp, S. L. S.; Refson, K. *J. Chem. Phys.* **2004**, *121*, 8511.

(29) Sudarsan, K.; Young, R. A. *Acta Crystallogr., Sect. B: Struct. Crystallogr. Cryst. Chem.* **1969**, *25*, 1534.

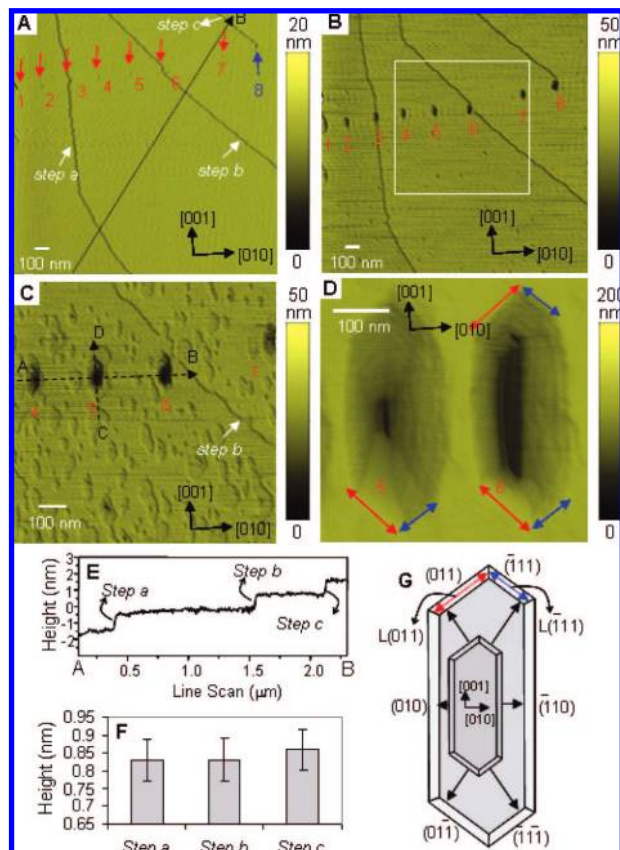


Figure 2. Structural characterization of HAP (100) surfaces during the dissolution processes. (A) AFM image of (100) surface before adding acidic buffer. White arrows indicate the step location from steps a, b and c. Black arrows indicate edge dislocation sites (numbers from 1 to 7). A blue arrow indicates the screw dislocation site (number 8). (B) AFM image 5 min after injection of citrate buffer. (C) White boxed region in Figure B (35 min later). Two arrows (A to B and C to D) represent line scan regions in panels A and BB of Figure 2, respectively. (D) Asymmetric shape of etch pit 5 and 6 (90 min later). (E) Line scan from A to B in Figure 2A. (F) Average heights of steps a–c (0.83, 0.83, 0.86 nm, respectively) from 50 measurements across each step. Error bars represent standard deviations. (G) Model of evolution of the hexagonal etch pit. Arrows represent relative step velocities displaying different facets.

which the long axis of the hexagons ran parallel to the [001] direction (Figure 2D and G). On the (100) HAP surfaces without defect structures, many new flat-bottomed pits were formed randomly on the flat terrace having single $d(100)$ depths (Figure 2C). Pits were homogeneously distributed over the entire surface temporally and spatially, suggesting that flat-bottomed pit formation proceeded stochastically (Figure S1). The overall dissolution rate was mainly governed by propagation of the defect initiated elongated hexagonal etch pits, which provided the major source of steps³⁰ (Movie S1). The dissolution rates estimated from the vertical retraction at defect sites and flat terrace regions were $4(\pm 3) \times 10^{-8}$ and $4(\pm 5) \times 10^{-9}$ mol/m²·s, respectively.

The shape of etch pits originating from defect sites were governed by the surface symmetry of HAP. During dissolution, the etch pits displayed reflectional symmetry across the [010] direction, but not across the [001] direction (Figure 2D, G). This etch pit symmetry is identical to the model (100) surface symmetry of HAP (Figure 3D). Cross-sectional analysis of AFM images along the [001] direction exhibit mirror symmetry as the etch pit evolves (Figure 3B). However, cross sectional analysis along

the [010] direction shows that during dissolution the slopes of the left facets were steeper than those of the right facets, and the deepest point of the initial etch pits were inclined toward the left side, not in the middle (Figure 3A). Because retraction of individual steps proceeded independently, the differing slopes must have originated from different step retraction velocities, with steps displaying $(\bar{1}10)$ facets having faster step velocities than steps displaying the (010) facets (Figure 3C and E). We confirmed the step velocity differences by measuring the displacement of each facet from the initial pinhole positions along six different directions and calculating their step velocities (Figure 3C). In addition, the steps displaying $\{\bar{1}11\}$ facets retracted at higher velocities than those displaying $\{011\}$ facets resulting in shorter $\{\bar{1}11\}$ facet lengths ($L_{\{\bar{1}11\}}$) than the $\{011\}$ facet lengths ($L_{\{011\}}$) (red and blue arrows in Figure 2D and G).

The asymmetric features were observed in all of the etch pits, regardless of the sample chosen. The asymmetry was consistent on all pits for any given HAP crystal (Figure 2D and Movie S1) while scans of other crystals showed either the same pit symmetry or mirrored symmetry across the [001] direction. Additionally, the shape of the pits was independent of the scanning directions implying that the asymmetry was not an AFM tip-induced artifact. Moreover, the asymmetry was observed not only in defect induced etch pits but also in the flat bottom pits on the terrace regions. Furthermore, the same features were also observed using a different buffer (piperazine-*N,N'*-bis(2-ethanesulfonic acid) buffer), reassuring us that the asymmetry was not due to specific interactions between the conjugate base of the acid buffer with the HAP surface (Figure S2). Thus, the pit morphology was a property of the underlying HAP crystal structure.

The consistent observation of asymmetric etch pits can be used to predict the absolute crystallographic configurations of the HAP crystals. We calculated the step energies of $d(100)$ height steps displaying (010) and $(\bar{1}10)$ facets (Figure 3E). This calculation predicts that steps with $(\bar{1}10)$ facets were energetically less stable than steps with (010) facets. The step energies for the (010) and $(\bar{1}10)$ facets were 4.00×10^{-10} and 7.68×10^{-10} J/m, respectively. Although these static equilibrium calculations apply to samples in vacuum, they do serve to illustrate a calculable difference between the energetic properties of the two very similar step types. Consequently, steps displaying the $(\bar{1}10)$ face are energetically disfavored, and we hypothesize that they could be more susceptible to dissolution. These results are consistent with the crystallographic orientations assigned in Figure 2G.

Hexagonal etch pit formation has previously been observed in various biological apatites^{31–33} but has not been correlated with the underlying crystallographic structure. Because bone resorption takes place under the osteoclast cell membrane, there is no tool for studying how the structural characteristics of HAP affect dissolution in real time. In contrast to the pH at which bone resorption occurs physiologically (pH 4.5),³⁴ the pH at which our HAP was dissolved (pH 6.0) was much milder. This pH was chosen in order to achieve dissolution rates which were compatible with the time resolution of AFM. However, the final morphologies that formed at pH 4.5 were very similar to those produced at pH 6.0. Therefore, our observations are relevant for understanding the resorption of healthy and defected bone sites.

We report the first comprehensive characterization of the real-time dissolution of (100) HAP surfaces bearing various structural defect structures using in situ AFM. We found that tiny local

(31) Dorozhkin, S. V. *J. Cryst. Growth* **1997**, *182*, 125.

(32) Daculsi, G.; Legeros, R. Z.; Mitre, D. *Calcif. Tissue Int.* **1989**, *45*, 95.

(33) Voegel, J. C.; Frank, R. M. *Calcif. Tissue Res.* **1977**, *24*, 19.

(34) Silver, I. A.; Murrills, R. J.; Etherington, D. J. *Exp. Cell Res.* **1988**, *175*, 266.

(30) Lasaga, A. C.; Lutge, A. *Science* **2001**, *291*, 2400.

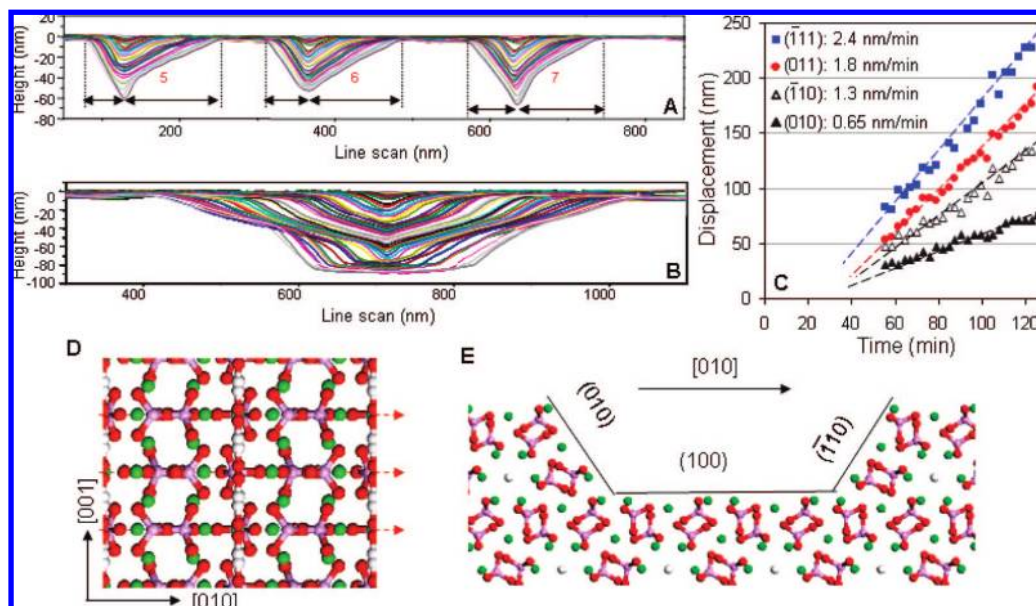


Figure 3. Asymmetric etch pit evolution relative to the symmetry of HAP surface and the model of HAP. (A and B) Time-dependent vertical depth profile along [010] and [001], respectively. Time interval of each line is 175 s. Line scan areas are shown in Figure 2C. (C) Step displacements from the initial dislocation point to each facet. Step velocities displaying (011) or (01 $\bar{1}$), ($\bar{1}$ 11) or ($\bar{1}$ 1 $\bar{1}$), ($\bar{1}$ 10), and (010) are 2.4, 1.8, 1.3, 0.65 nm/min, respectively. (D) Symmetry of the (100) surface. Mirror plane are indicated across the [010] direction (red arrows). (E) View through the [001] direction showing a hypothetical etch pit in the (100) surface. The exposed step faces can be seen to be unequivalent owing to the opposite orientations of the phosphate groups.

structural defects significantly affect the overall dissolution rate. This may serve as a good model for comparing the dissolution processes of defected bones with healthy bones in resorption processes. Our molecular level description of dissolution on well-defined HAP crystal surfaces will provide useful insights for the design of the novel therapies for treating osteoporosis, dental caries, and many bone- and tooth-related diseases.

Acknowledgment. We thank Dr. James De Yoreo for helpful discussions. This work was supported by National Science Foundation Early Career Development Award (DMR-0747713),

start-up funds from the Nanoscience and Nanotechnology Institute at the University of California, Berkeley (SWL), the Laboratory Directed Research and Development fund from the Lawrence Berkeley National Laboratory.

Supporting Information Available: A dissolution AFM movie, AFM images for stochastic generation of flat-bottom-etch pits and AFM images of etch pits in pH 6.0 piperazine- N,N' -bis(2-ethanesulfonic acid) buffer. This material is available free of charge via the Internet at <http://pubs.acs.org>.

LA801735C